Nanoscale

DNA Conductance Modulation via Aptamer Binding

Journal:	*Nanoscale*
Manuscript ID	NR-ART-12-2024-005139.R1
Article Type:	Paper
Date Submitted by the Author:	17-Feb-2025

Complete List of Authors:	Mohammad, Hashem; Kuwait University College of Engineering and Petroleum, Electrical Engineering Alsaleh, Lina; Kuwait University, Department of Electrical Engineering Alotaibi, Abrar; University of Leeds Alolaiyan, Olaiyan; University of Washington, Department of Electrical and Computer Engineering Takahashi, Taisei; Institute of Science Tokyo, Department of Chemistry Anantram, M P; University of Washington, Department of Electrical Engineering Nishino, Tomoaki; Institute of Science Tokyo, Department of Chemistry

DNA Conductance Modulation via Aptamer Binding

Hashem Mohammad[1*], Lina Alsaleh[1], Abrar Alotaibi[2], Olaiyan Alolaiyan[3,4], Taisei Takahashi[5], M.P. Anantram[3], and Tomoaki Nishino[5].

[1] Department of Electrical Engineering, Kuwait University, P.O. Box 5969, Safat 13060, Kuwait.

[2] School of Electronic and Electrical Engineering, University of Leeds, Woodhouse, Leeds LS2 9JT, United Kingdom.

[3] Department of Electrical and Computer Engineering, University of Washington, Seattle, Washington 98115, United States

[4] Center of Excellence for Green Nanotechnologies, Microelectronics and Semiconductor Institute, King Abdulaziz City for Science and Technology, Riyadh, Saudi Arabia, 11442.

[5] Department of Chemistry, School of Science, Institute of Science Tokyo, 2-12-1 W4-10 Ookayama, Meguro-ku, Tokyo 152-8551, Japan.

[*] Corresponding author

1 Abstract

The electronic properties of DNA make it an attractive candidate for applications in biosensing and molecular electronics. One approach to utilizing DNA in these fields involves binding molecules, such as aptamers, to control DNA's electrical conductance. By combining molecular dynamics simulations and density functional theory with Green's function-based charge transport calculations, we gain insights into aptamer induced structural realignment of DNA base pairs near the binding site. We find that this structural

realignment enhances the electronic coupling, creating a conductive path near the highest occupied molecular orbital. This interaction results in a significant modulation of conductance by at least an order of magnitude compared to the dsDNA without the aptamer. We anticipate that our findings will promote the development of DNA-aptamer complexes for use in molecular electronics and biosensing applications.

Keywords*: DNA, Aptamer, Green's function, DFT, charge transport.*

2 Introduction

In recent years, the modulation of DNA's electrical conductance has garnered significant interest due to its distinctive structural and electrical properties. DNA's sequence-specific base-pairing and self-assembly capabilities have been leveraged to construct two-dimensional and three-dimensional structures using a bottom-up approach [1–3]. Additionally, DNA can conduct electrical current, which is influenced by both its sequence and molecular alterations within the strand [4–10]. DNA's ability to bind with organic and inorganic molecules further enables the modification of its electronic properties [11–20]. To functionalize nucleic acids while preserving DNA's core benefits (base-pairing and charge transport), several approaches have been explored. One strategy is chemically modifying DNA to enhance its structural stability and nuclease degradation. Examples include peptide nucleic acids (PNA)[21], where the phosphate group in the backbone is replaced with peptides, and the 2′-deoxy-2′-fluoro-arabinonucleic acid (2′F-ANA)[22], where a fluorine replaces hydrogen on the sugar's 2' carbon. Another example is to expand the DNA bases by the addition of benzene ring (xDNA)[23,24] , which increases surface area, thermal stability, and reduces HOMO-LUMO gaps.

The applicability of different techniques to alter DNA opens open new opportunities for utilizing DNA as a molecular device and electrical biosensor [14,18,25–30]. From an electronics perspective, tuning nanostructures to achieve substantial conductance contrast is essential for the development of advanced devices. By designing DNA nanostructures with a significant conductance variation across different strands, it may be possible to pave the way for future memory devices and bio-inspired interconnects [25,31,32].

One approach to altering DNA conductance is by utilizing aptamers, which are short nucleic acid sequences designed to bind with high affinity and specificity to target molecules [33–36]. Aptamers, such as G-quadruplex structures, extend the range of targets to include non-nucleic acid molecules, enabling the detection of biomarkers for health, environmental and food safety monitoring [33,37,38]. In the context of molecular electronics, the charge transport properties of G-quadruplexes have been explored both theoretically and experimentally [30,39,40]. However, the intrinsic aptamers' effect on DNA conductance has yet to be fully understood.

In this study, we conduct fundamental investigations on a G-quadruplex (5'-GGTTGGTGTGGTTGG-3') aptamer (Gquad) linked to double-stranded DNA (dsDNA) via a short 5'-TTTAA-3' bridge, a sequence known for its high stability [37]. We employ combination of molecular dynamics (MD) simulations, density functional theory (DFT), and Green's function-based quantum charge transport calculations to model the system in a contact-DNA-contact setup. Our results show that the terminal conductance of the aptamer-mediated DNA differs significantly from that of the equivalent structure without the aptamer. We find that the presence of the aptamer can lead to over an order of magnitude difference in conductance, offering a potential pathway for developing DNA strands with substantial resistance contrast.

3 System Under Study

Following the sequence design of DNA-aptamer structure reported in [41], we propose a 12 base-pair long DNA strand that binds with the aptamer via a binding-site sequence similar to that in reference[41] to investigate the electrical properties of the system and fundamentally understand the effect of attaching the aptamer. We employ a combination of molecular dynamics (MD), density functional theory (DFT), and quantum charge transport calculations based on Green's function approach. We simulate a dsDNA with the sequence 5'-GCGCCG**CGTC**CC-3' that is in a contact-DNA-contact setup with and without the aptamer as shown in Figure 1. We note that we maintained the dsDNA binding site sequence (in bold) as in [41]. We

opted to change the rest of the DNA sequence to be GC-rich to favor charge transport and enhance conductance along the DNA.

The conformation of the dsDNA can be found in multiple forms depending on the solvent environment [9,42–44]. B-form DNA is mainly found in high dialectic solvents such as water, which has a dielectric constant of 78.4. G-quadruplexes are secondary structures formed by guanine-rich sequences [4546]. Their formation is often facilitated by the presence of cations, which stabilizes the G-quadruplex structures. Monovalent cations -mainly K^+ and Na^+- can stabilize specific G-quadruplex strands [47–49]. It was noted that increasing the Na^+ concentration stabilizes antiparallel G-quadruplex structures [50]. In this study, we model the system in water with Na^+ as the counterions present in solution. Thus, we built the DNA-aptamer system by using B-form dsDNA and anti-parallel G-quadruplex structure for the dsDNA and aptamer, respectively. In a solvent environment and room temperature operation, DNA is considered a soft floppy molecule as it constantly interacts with the surrounding water and counterions. Therefore, in modeling charge transport, we include decoherence to incorporate phase-breaking scattering events that occur to the electron as it traverses the DNA and interacts with the environment.

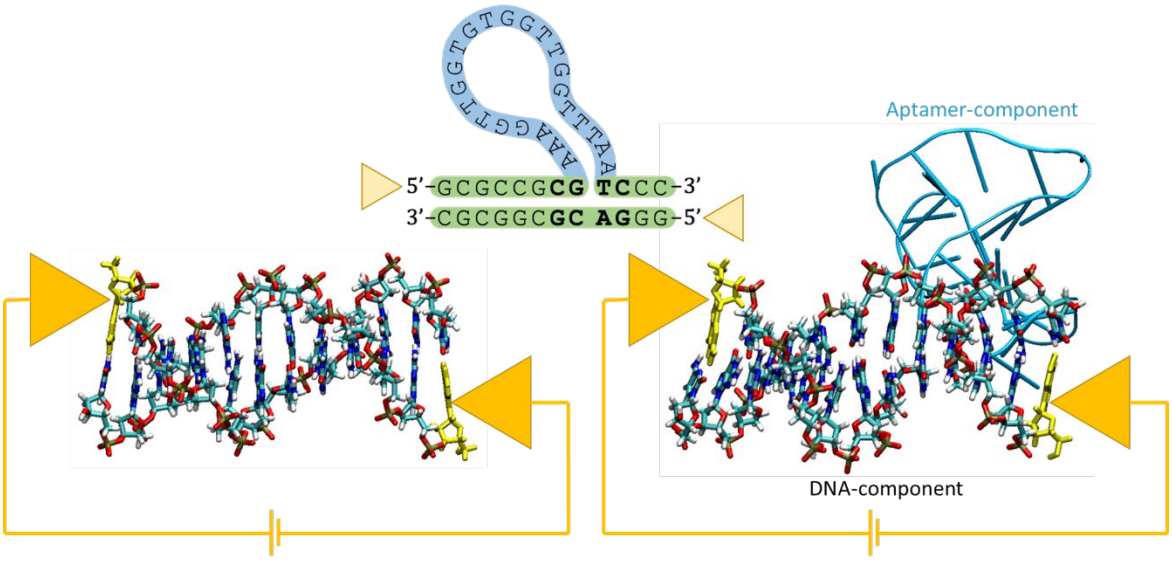

Figure 1 DNA system under study in the contact-DNA-contact setup. Two systems are studied: ds-DNA with and without the aptamer (blue). The yellow colored nucleotides represent the location of the contacts self-energy for charge transport calcualtions.

4 Methods

The construction of the DNA-aptamer structure involves three structures: A 15-mer G-quadruplex with the sequence 5'-GGTTGGTGTGGTTGG-3' (Figure S1 (a)) sourced from the PDB Database (PDB ID: 148D); A 12-mer dsDNA with the sequence 5'-GCGCCGCGTCCC-3' created in B-form DNA using Avogadro [51](Figure S1 (c)); and a double-stranded 5'-TTTAA-3' sequence to bridge the G-quad and DNA together (Figure S1 (b)). The ds-TTTAA DNA was generated in B-form using Avogadro, and then imported into GaussView [52], where the complementary thymine bases to the AA-3' proximal to the dsDNA were removed, and a phosphate group (PO_3) was manually added to the terminal O3' of the 3'-end Adenine (Res ID: A_5). First, all three structures—G-quadruplex, TTTAA, and the dsDNA—were individually energy minimized using Amber [53] in an implicit water solvent model. After combining the three structures, we ran 100 ns MD simulations with explicit solvent on the full DNA+aptamer structure, followed by single-point DFT and charge transport calculations. The detailed steps for generating the DNA+aptamer structure are provided in the supplementary information.

4.1 MD Simulation

The structural preparation of the DNA-aptamer was carried out in AMBER[53] using the DNA.bsc1 force field [54]. The system was solvated in a cubic box with the TIP3P [55] water model and a 15 Å buffer. To neutralize the structure, 45 sodium ions (Na^+) were added.

The molecular dynamics simulations were conducted in five stages. First, the system underwent two energy minimization steps: one with restraints on the DNA-aptamer to relax the solvent and ions, and a second targeting the entire system without restraints. Both minimizations used a non-bonded cutoff of 10.0 Å. The heating phase raised the system's temperature from 0 K to 300 K over 1 ns under constant volume (NVT) conditions, with restraints applied to the DNA-aptamer structure. During equilibration, the system was further relaxed for 1 ns under constant pressure (NPT) with reduced restraints. The final production run, conducted under constant pressure (NPT) conditions, lasted for 100 ns, during which all restraints were

removed. The SHAKE [56] algorithm was applied throughout to constrain bonds involving hydrogen atoms, and the Particle Mesh Ewald (PME) [57] method was used for long-range electrostatics.

To analyze the electronic properties of the DNA-aptamer structure, we utilized an RMSD-based clustering algorithm within VMD [58], categorizing the conformations observed during the simulation. A cutoff value of 4 Å was used to cluster the DNA-aptamer structure. We then selected the centroid structures from the most populated cluster, representing the conformations with the minimal RMSD difference from others in the top cluster. The selected structures were then minimized prior to the DFT calculation step to help with convergence. The clustering figures and tables are provided in the supplementary information along with additional notes on the effect of minimization on charge transport results.

The clustering of pristine DNA shows that more than 90% of the conformations belong to the top cluster (see table S1 and table S2 in supplementary information). For the DNA+aptamer structure, 68.3% of conformations are classified under the top cluster, with 25% belonging to clusters 2 and 3. In our study, we focus the analysis on the most probable conformation, cluster 1, however, we also include results of clusters 2 and 3 in the supplementary for the DNA+aptamer.

4.2 DFT Calculations

We used Gaussian 16 [59] to run single-point energy calculations on the representative structures from the previous step. We imported the DNA-aptamer structure from the MD step and stripped it from water and counterion molecules. In a previous study [60], we found that the high dielectric constant of water solvent screens the effect of surrounding counterions. Their effect was found to mainly add energy levels deep in the unoccupied orbitals region, which is far from our energy range of study. The resulting DNA+aptamer size is 1500 atoms. We modeled the system using B3LYP hybrid functional with 6-31G(d,p) basis set. We included the solvent effect using the conductor polarizable continuum model (C-PCM), which is found to yield good results for modeling DNA in water [61–63]. Especially with the large system size, this approach gives us a good balance between accuracy and computational complexity. We note that recently, Teo and coworkers [64] have benchmarked several DFT functionals to study DNA charge transport. They used the

results of CASSCF and CAS-PT2 calculations that include 11 electrons in 12 orbitals as benchmark values for the effective electron coupling. They reported that B3LYP results in excessive delocalization of the valence charge and overestimation of the effective electron coupling when compared with other functionals that have higher percentages of HF exchange component. Thus, they recommend functionals that include higher HF exchange component to better describe the long-range interactions. While our approach in this work relies on B3LYP, this warrants further discussions in the future to investigate the choice of functionals on the DNA charge transport results. The DFT calculations result in the Fock and Overlap matrices, which we then use in the next step for the charge transport calculations.

4.3 Quantum Charge Transport Calculations

We model the system in a contact-DNA-contact setup as shown in Figure 1. We refer the reader to [65] for the details of the charge transport model and will only mention the main points here. After obtaining the Fock (F) and Overlap (S) matrices from DFT, we use Löwdin transformation [66] to generate the system Hamiltonian (H_0) as follows,

$$H_0 = S^{-\frac{1}{2}} F S^{-\frac{1}{2}} \tag{1}$$

Following our approach in[65], we partition the DNA into nucleotides (backbone + base), where nucleotide m corresponds to the partition labeled m.

Let H_{0m} represent the diagonal blocks of H_0 corresponding to nucleotide m, and u_m is a diagonal sub-matrix consisting of the eigenvectors of H_{0m}. We define the matrix U to be

$$U = \begin{bmatrix} u_1 & 0 & \cdots & 0 \\ 0 & u_2 & & \\ \vdots & & u_m & \\ & & & \ddots \\ 0 & \cdots & & u_N \end{bmatrix} \tag{2}$$

where N is the total number of nucleotides in the DNA and the dimension of u_m is O_m, and,

$$O_m = \sum_{i=1}^{N_m} b_i \tag{3}$$

is equal to the total number of basis functions (O_m) used to represent nucleotide m. N_m is the total number of atoms in nucleotide m. Then, the unitary transformation,

$$H = U^{\dagger} H_0 U \tag{4}$$

diagonalizes the diagonal blocks corresponding to each nucleotide m. The diagonal blocks of H are now diagonal matrices. The diagonal elements of the diagonal blocks represent the eigenvalues of that nucleotide. The off-diagonal blocks of H represent the hopping parameters between the molecular orbitals of the nucleotides. The size of each diagonal

block corresponding to nucleotide m is equal to O_m. We then use H as input for the Green's function approach of charge transport calculations with energy-depended decoherence.

The model requires finding the retarded Green's function term of the DNA by including the self-energies of the contacts and the decoherence,

$$[E - (H + \Sigma_{\mathrm{L}} + \Sigma_{\mathrm{R}} + \Sigma_{\mathrm{B}})]G^r = I \tag{5}$$

where E is energy, I is the identity matrix, H is the diagonalized Hamiltonian. The term $\Sigma_{L(R)}$ is the left (right) contact self-energy, which includes the effect of having two contacts attached to the DNA. We model the effect of having semi-infinite gold electrodes connected to the DNA as self-energy within the Green's function formalism. Previous work has shown that for gold contacts, applying the wide-band limit to represent the self-energy as an energy-independent coupling parameter is sufficient [67]. This approach includes the level broadening due to contacts, where $\Sigma_{L(R)}$ is a diagonal matrix defined as $\Sigma_{L(R)}(E) = -i\frac{\Gamma_{L(R)}}{2}$. The term Γ represents the scattering strength of electrons in and out of the DNA at the left(right) contact sites. The last term, Σ_B, is the decoherence self-energy. It is similar to the contacts self-energy but taken to be energy dependent. The diagonal elements of the Σ_B matrix are given by,

$$\Sigma_B(E) = -i\frac{\Gamma_{k,m}(E)}{2} \tag{6}$$

where $\Gamma_{k,m}$ represents the coupling strength between the decoherence probe and molecular orbital k of nucleotide m. It is defined as

$$\Gamma_{k,m}(E) = \Gamma_B \times \exp\left[-\frac{|E-\epsilon_{k,m}|}{\lambda}\right] \tag{7}$$

where Γ_B represents the maximum scattering strength, $\epsilon_{k,m}$ is the molecular orbital k of nucleotide m, and λ dictates the exponential decay of decoherence off-resonance.

The density of states can be found from the retarded Green's functions

$$DOS(E) = -\frac{Im[diag[G^r(E)]]}{\pi} \tag{8}$$

The low-bias conductance of the system can be found by

$$G\left(E_f\right) = \frac{2e^2}{h}\int dE\, T_{eff}(E)\frac{\partial f\left(E-E_f\right)}{\partial E} \tag{9}$$

where E_f is the Fermi energy, e is the electron charge, h is Planck's constant, T_{eff} is the effective electron transmission probability with decoherence (see references [65,68,69] for full proof), and $f\left(E-E_f\right) = \left[1+\exp\left(\frac{E-E_f}{kT}\right)\right]^{-1}$ is the Fermi function, k is Boltzmann constant and T is temperature.

In the current work, our goal is to investigate the effect of aptamer binding to DNA, so we assumed that both systems (pristine DNA and DNA+aptamer, respectively) have the same contacts setup (location and coupling value). This helps us reduce the variability and focus on the inherent transport properties of the two systems. In our previous [65], we tested several values of contacts coupling that extend from 10 to 10,000 meV and found that around 600 meV the transmission becomes less dependent on the contact coupling strength. Therefore, the coupling in the current study is set as $\Gamma_{L(R)} = 600\ meV$ to minimize the contacts resistance effect. We also assumed the electrodes are coupled with the DNA nucleotides to be consistent with previous work reported in literature. Following our previous work [65], we set the remaining transport

calculation parameters to $\Gamma_B = 100\,meV$, $\lambda = 50\,meV$, and $kT = 0.0259\,eV$ (i.e., room temperature operation). These values were determined to yield conductance that quantitatively agree with those reported experimentally. We also set the contacts self-energy to be at the 5'-ends guanines to maximize the transmission within the HOMO energy range [32,70,71]. In the following when discussing the results, we will refer to DNA without aptamer as *dsDNA*, and DNA+aptamer structure as *dsAPT*.

5 Results and Discussion

5.1 MD Results Analysis

The RMSD analysis of the DNA+aptamer system in Figure 2 shows a conformational change throughout the MD simulation. The RMSD plot in Figure 2 represents a 2D matrix where both axes correspond to time frames of the simulation (0 to 100 ns). The x-axis represents the simulation frames being analyzed, and the y-axis represents the reference frames against which these are compared. Each point on the matrix corresponds to the RMSD value (in Å) between a simulation frame (x-axis) and a reference frame (y-axis). The color bar indicates the magnitude of structural deviations. The RMSD in Figure 2(a) indicates approximately four distinct clusters, suggesting periods of stability at various points in the simulation. When analyzing RMSD separately for the DNA and aptamer components (Figure 2(b) and (c), respectively), we observe that the aptamer's RMSD trend closely mirrors that of the full structure, although with significantly lower RMSD values. In contrast, the DNA component remains largely stable, with only minor conformational shifts occurring. These results suggest that the observed conformational changes in the overall system are primarily due to the aptamer, with having both DNA and aptamer we have larger structural size contributing to the higher RMSD values seen in the full system.

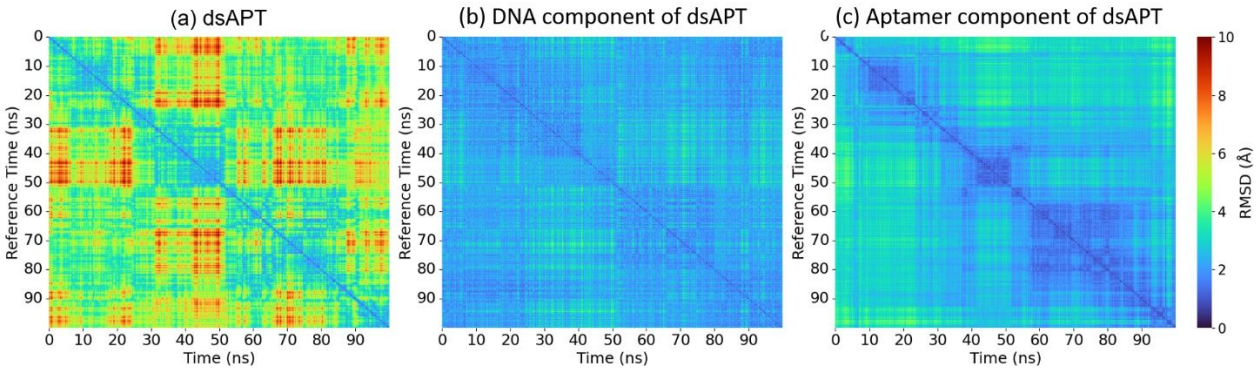

Figure 2 RMSD plot of the simulation frames for DNA+aptamer within the 100 ns MD simulation used for clustering the conformations. (a) RMSD for the whole DNA+aptamer structure, (b) RMSD for only the DNA component, and (c) RMSD for only the aptamer.

The RMSD plot for the dsDNA (without an aptamer) is provided in Figure S7. Comparing the plots for dsDNA and the DNA-component of the DNA+aptamer in Figure 2 (b) indicates that both structures remain stable across the MD simulations, with only minor conformational shifts. Notably, the dsDNA structure exhibits slightly higher stability, which is expected given the absence of additional interacting components that could influence its conformational stability.

To accurately capture the fluctuations of each structure individually, we measured the root mean square fluctuation RMSF for the aptamer and DNA components separately, rather than analyzing the full dsAPT structure together. When aligning the full system, the RMSF values ranged between 2 and 5 Å, as shown in Figure S9, which does not fully reflect the individual fluctuations of each component. Therefore, we reanalyzed the RMSF separately for a clearer comparison. For the aptamer component, shown in Figure 3(a), the RMSF values mostly range between 1 and 2 Å, indicating overall structural stability. However, a notable peak appears between atoms 180 and 190, where the fluctuation reaches slightly above 6 Å. This corresponds to the thymine region T_{14} at the top of the G-quadruplex aptamer, as referenced in Figure S10. This high flexibility occurs far from the DNA binding sites, suggesting that the observed structural dynamics are intrinsic to the aptamer and not influenced by DNA binding. For Figure 3(b), the comparison between the DNA-component of dsAPT and the pristine DNA (dsDNA) reveals that both structures exhibit similar fluctuation patterns, with the dsDNA showing slightly lower fluctuations. This is expected, as the

pristine DNA remains unbound, whereas DNA-component of dsAPT interacts with the aptamer-component, potentially causing slight structural adjustments. We observe higher fluctuations in specific regions, particularly at the base pair terminals: atoms numbers 1–34, 343–404, and 726–755, where the RMSF reaches around 3 Å. The remaining structure exhibits fluctuations mostly between 1 and 2 Å, indicating overall stability. Comparing the two individual components of dsAPT, the DNA-component appears more stabilized than the aptamer-component. This aligns with our previous RMSD analysis, where the aptamer-component exhibited higher conformational changes.

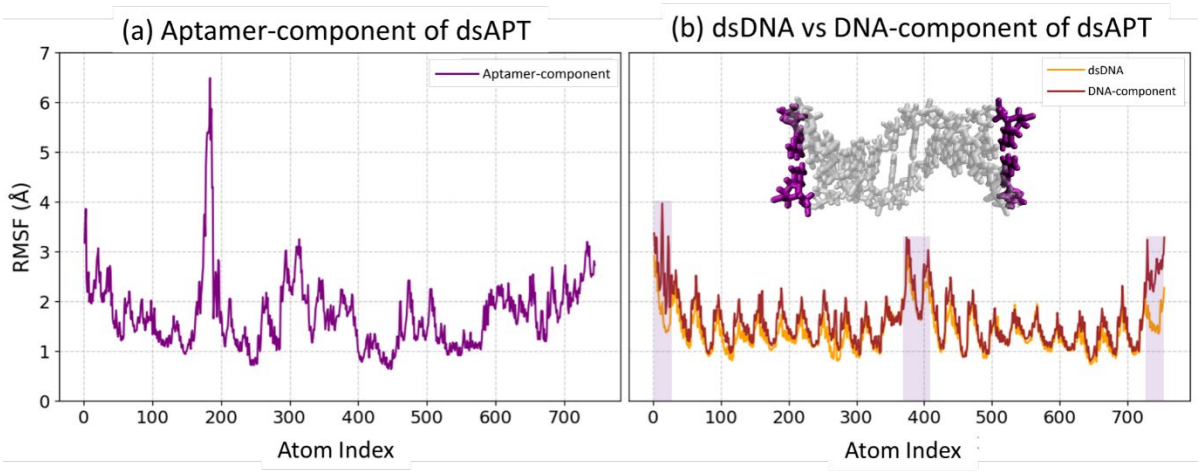

Figure 3 RMSF of (a) Aptamer-component of dsAPT, (b) dsDNA and DNA-component of dsAPT. The purple shaded regions in (b) highlight the atom numbers with high RMSF value which corresponds to terminal bases colored in purple.

5.2 Transmission and Conductance

We note that for the charge transport and conductance calculations, we did not calculate the Fermi Energy (E_f). Determining the exact Fermi energy of the contact-DNA-contact system is not an easy task because it requires self-consistent calculations that involve accounting for the contact details (atoms geometry), solving and Poisson's equation. As an alternative approach suggested by Zahid et al. [72], we treat the Fermi energy as a fitting parameter and sweep the energy when we plot the transmission (or conductance). When modeling DNA conductance in a two-terminal contact-molecule-contact setup, we expect the Fermi energy of the contacts to be in the bandgap closer to the HOMO of the molecule. This comes from comparing the workfunction of gold contact with the ionization potential of DNA nucleotides, and the occurrence of partial

charge transfer between the contacts and DNA [5,16,32]. Therefore, in this work, we will focus our analysis on an energy window close to the HOMO.

The energy levels distribution and transmission profile are shown in Figure 4 and Figure 5. Both systems resemble wide-bandgap semiconductors, with bandgap values of 3.89 eV for dsDNA and 3.95 eV for dsAPT. We notice that the addition of aptamer shifts the HOMO and LUMO to higher energies by 27 meV and 81.6 meV, respectively. Further, the aptamer yields 193x higher transmission around the HOMO (~-4.8 eV) than the pristine dsDNA.

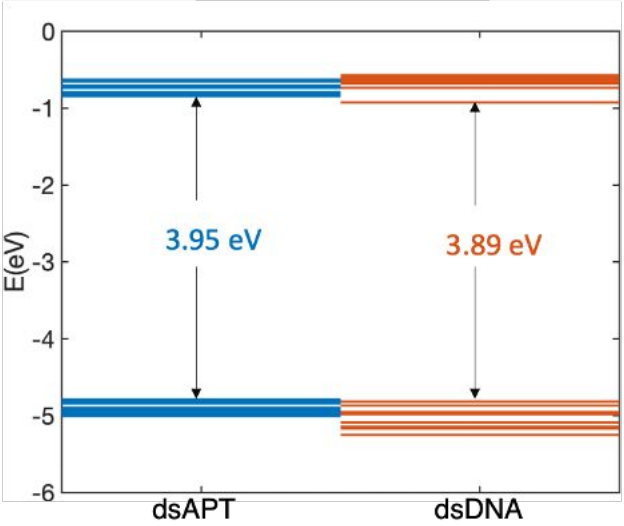

Figure 4 Overall energy levels distribution of DNA+aptamer (dsAPT) and dsDNA.

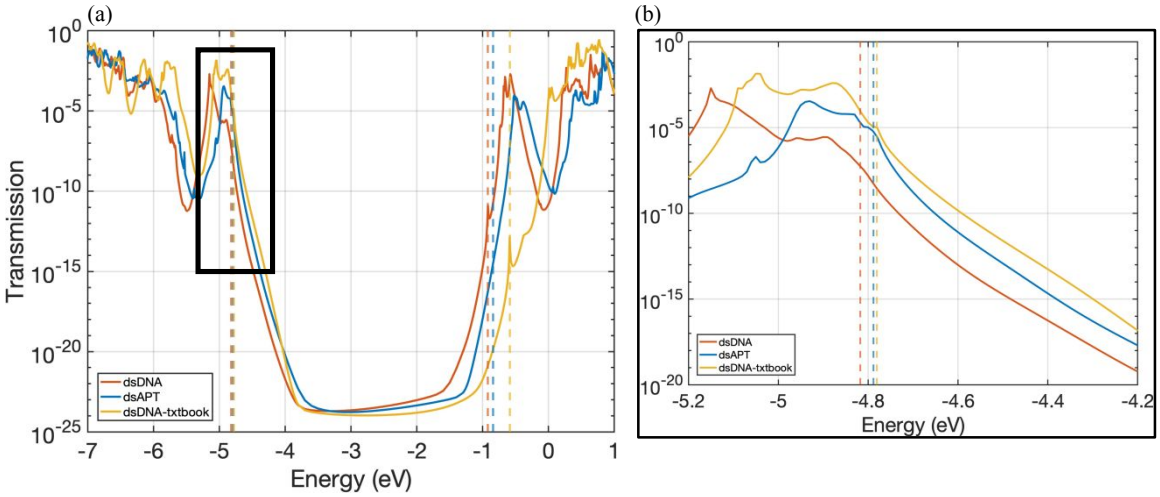

Figure 5 (a) Transmission profile extending from HOMO to LUMO regions. (b) The zoom-in window from the HOMO edge into the bandgap. The dashed colored lines correspond to HOMO and LUMO of each structure.

We then calculated the low-bias conductance using equation (9), which yielded $G(HOMO_{dsDNA}) = 0.55$ μ G_0, and $G(HOMO_{dsAPT}) = 26$ μG_0, where $G_0 = 7.74 \times 10^{-5}$S is the conductance quantum.

As shown in Figure 6, the aptamer increases conductance by at least 47 times within the Fermi energy window from HOMO to the bandgap. Experimentally, previous work on 8 bps long DNA strands modified with binding molecules have reported to have conductance within the range of $72\mu G_0 - 3.5\ mG_0$ [15,18]. Additionally, Guo et al. reported conductance of 11 bps long modified DNA with intercalator in the range of $2.7 - 10\ \mu G_0$ [14]. Our previous work in modeling DNA conductance modulation via anthraquinone intercalation yielded a maximum of 4 times increase in conductance [16]. Therefore, the current results present us with a promising conductance modulation method to increase the conductance of a 12 bp long DNA.

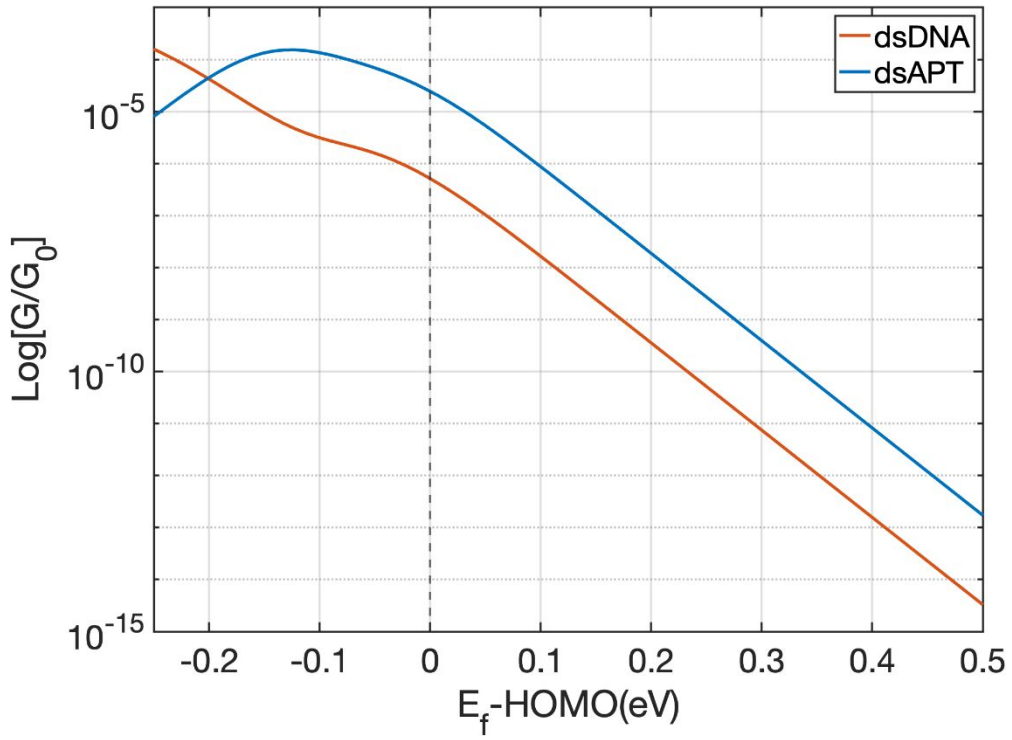

Figure 6 Conductance as a function of Fermi energy shifted with respect to HOMO.

The dsDNA without the aptamer exhibits a low conductance of 0.55 μG_0 (42.5 pS). AT base pairs, with higher ionization potential than GC pairs [73,74], act as energy barriers in charge transport, while GC pairs form the main conduction pathway in the occupied orbitals region [32,70,71]. Previous studies also report conductance in the pS-nS range for AT-containing dsDNA [4,5,16,75]. We also compared dsDNA conductance before and after MD simulations, which reveals significant differences: the textbook B-DNA structure shows a much higher conductance (342 μG_0, 620 times greater than dsDNA after MD, see supplementary figure S13). This suggests that low conductance in the MD-simulated dsDNA arises not only from presence of AT but also structural changes impacting energy levels distribution. The next section explores molecular orbital distribution and structural differences in greater detail.

5.3 Molecular Orbital Distribution and Structural Analysis

To gain further insights into why the aptamer increases the conductance, we next investigate the molecular orbitals' (MOs) distributions. First, we plot the wavefunctions[76,77] of the orbitals generated from DFT calculations in HOMO region closer to the bandgap edge, with energies between -4.9 eV and -4.8 eV. For the dsAPT structure, there are four MOs present within this energy window: HOMO to HOMO-3. However, there are only two MOs for the dsDNA structure: HOMO and HOMO-1.

Looking at the dsAPT structure in Figure 7 (left), we can see that HOMO-1 is the highest occupied MO localized at the aptamer-component, and it is far away from the DNA-component. *This shows that near HOMO, the highest occupied energy levels of the aptamer do not contribute to charge transport along the double-stranded DNA*. Further, HOMO, HOMO-2, and HOMO-3 are spatially distributed at the base-pairs segment $C_4C_5G_6C_7G_8$. The 2D DOS plot in Figure 8 (a) also shows that the MOs in this segment are energetically close, with an average energy difference of 55 meV (~2kT). One major effect of decoherence is to broaden the energy levels, hence, increasing the electron transmission off-resonance by making these levels with the ~2kT difference accessible to the electrons[65,78]. The combination of the spatial distribution of HOMO, HOMO-2, and HOMO-3 along the $C_4C_5G_6C_7G_8$ segment and the small energy separation creates a conductive path for the electron along the DNA-component near HOMO energy.

In contrast, the dsDNA without aptamer has two energy levels between -4.9 eV and -4.8 eV, separated by a large 4-bp gap (~1.45 nm), as shown in Figure 7 (right) and the red boxes of Figure 8(b). Moreover, unlike the dsAPT, the highest occupied MOs along the $G_6C_7G_8$ segment in the dsDNA create a ladder-like distribution with a 140 meV average energy separation (see arrows in Figure 8(b)). We expect this larger spatial and energy separation between the highest MOs to hinder charge transport and reduce transmission (conductance) near HOMO.

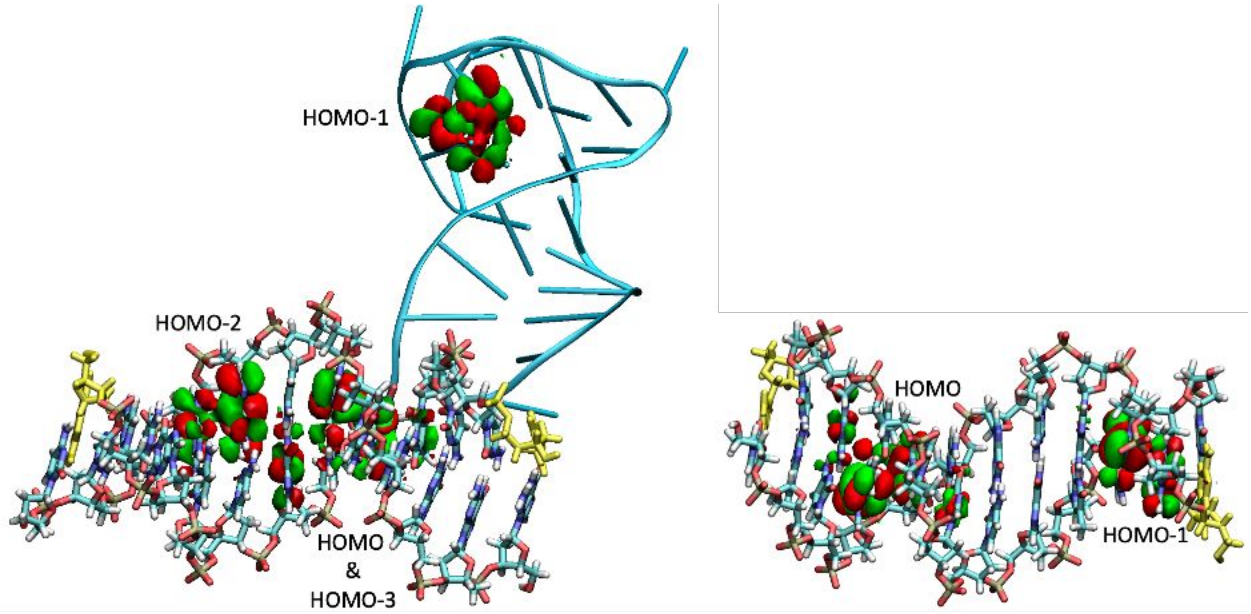

Figure 7 Wavefunction plots of HOMO-3:HOMO for dsAPT (left), and HOMO-1:HOMO for dsDNA (right). The ISO value is 0.01.

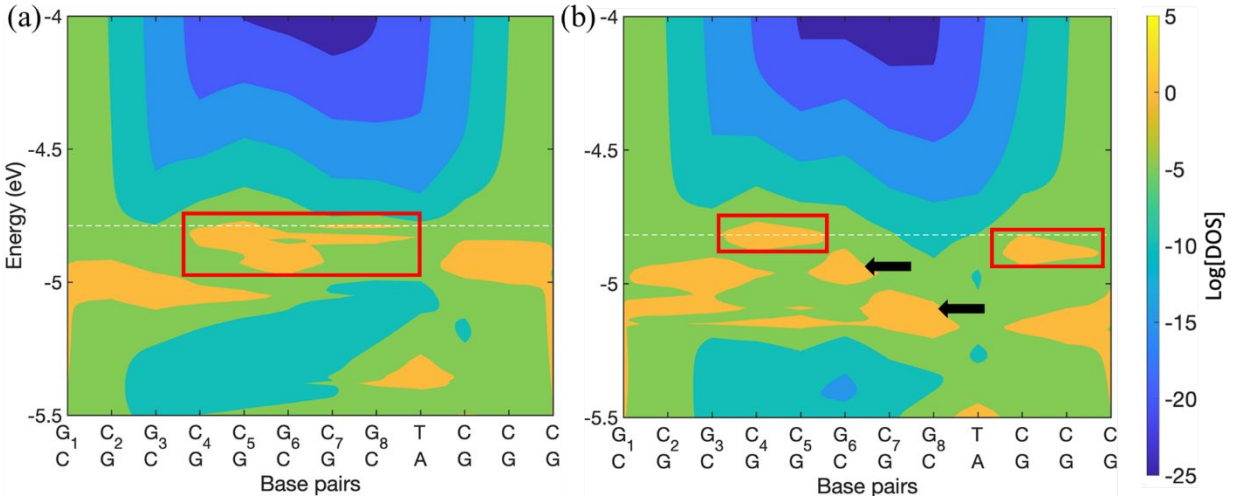

Figure 8 2D DOS plot of (a) dsAPT and (b)dsDNA alone. The localized DOS of the Aptamer was omitted for clarity. The red blocks highlight the molecular orbitals between -4.8 eV and -4.9 eV. The black arrows highlight the MOs of the $G_6C_7G_8$ segment (see main text for further details).

The MOs analysis shows that the aptamer does not directly contribute to charge transport via its localized HOMO, and that the orbitals of the $G_6C_7G_8$ segment play an important role. Considering the aptamer is attached at the backbones of G_8 and its neighboring thymine, we next investigate the structural effects of this attachment on the dsDNA, focusing at the $G_6C_7G_8$ segment. We analyzed the distance between the nearest neighbor base-pairs (rise) and the spatial overlap between them [79] in Figure 9. We also include the textbook B-DNA structure parameters as a reference. For simplicity, we refer to the base-pair comprised by the 6th guanine from the 5'-end and its complementary cytosine as (G_6C), and so on for the other bps. We can see in Figure 9 (a) that in the dsDNA case, G_6C and its neighboring C_7G bp are 4.75% farther away when compared with dsAPT, and the distance for dsAPT is almost matching the textbook B-DNA case. In contrast, the C_7G and G_8C are closer in the dsDNA case and farther apart when the aptamer is attached, with the aptamer increasing the separation by 9.4%. When compared with textbook B-DNA, the dsDNA with MD simulations has a rise value of 3.2 Å, which is 5% lower than the textbook B-DNA case (3.36 Å), whereas it is 3.5% higher for the dsAPT with respect to the textbook case. Finally, G_8C and its neighboring TA bp show 5.61% distance increase between dsDNA and dsAPT, which is similar to the textbook case. This draws an image that at the aptamer binding site, both and G_8C and TA are pulled closer together, increasing their spatial overlap by 30% as shown in Figure 9 (b). Also, it results in G_8C being pulled away from C_7G, reducing the overlap by 36.4%. Further, C_7G gets closer to G_6C, increasing the overlap by 58%. Overall, the binding of the aptamer results in the $G_6C_7G_8$ segment to have rise and overlap parameters resembling those of the textbook B-DNA.

We further used the Hamiltonian to extract the coupling between the localized HOMO of G_6C, C_7G, and G_8C bps. For this, we arrange the Hamiltonian from equation (1) in the order of the base-pairs,

$$H_o = \begin{bmatrix} H_{11} & H_{12} & \cdots & H_{1N} \\ H_{21} & H_{22} & & \vdots \\ \vdots & & \ddots & \\ H_{N1} & \cdots & & H_{NN} \end{bmatrix} \quad (10)$$

where N is the number of base-pairs (N = 12 for dsDNA, and N = 13 for dsAPT, with the aptamer treated as one block). The diagonal subblocks H_{qq} correspond to the Hamiltonian of base-pair q, and the off-diagonal subblocks H_{qp} represent the coupling between the base-pairs q and p. Then, we apply Equation **Error! Reference source not found.** (4) to perform the unitary transformation to diagonalize all H_{qq}. For this, U in Equation **Error! Reference source not found.** (2) is defined such that its diagonal subblocks U_{qq} $=$ eigenvectors(H_{qq}).

The diagonal subblocks of the resulting Hamiltonian contain the localized energy levels of each base-pair, and the off-diagonal subblocks correspond to the coupling (hopping strength) between energy levels on two different base-pairs. The coupling of localized HOMO for the $G_6C_7G_8$ segment bps are shown in Figure 9 (c). We find that after attaching the aptamer: 1) the HOMO coupling between G_6C and C_7G increases by 200 times from 0.2 meV to 40 meV. 2) In contrast, the HOMO coupling between C_7G and G_8C is reduced by 4.6 times from 102 meV to 22 meV. 3) The HOMO coupling between G_8C and TA is very low for all cases, this leads to AT creating an energy barrier for the $G_6C_7G_8$ segment. We can summarize the effect of the aptamer in Figure 10 as follows: the pulling of G_8C away from C_7G allowed C_7G to get closer to G_6C, which increases their HOMO coupling (π- π stacking). Although the distance has increased between C_7G and G_8C, their HOMO coupling did not diminish and is still appreciable (22 meV). As a result: C_7G now has an appreciable coupling with its nearest neighbors, which results in ~degenerate energy levels along the $G_6C_7G_8$ bp segment and at higher energies than the pristine case. To ensure the results are consistent throughout the conformations extracted from MD, we analyzed dsAPT structures from clusters 2 and 3 and they yielded the similar results (provided in the supplementary info).

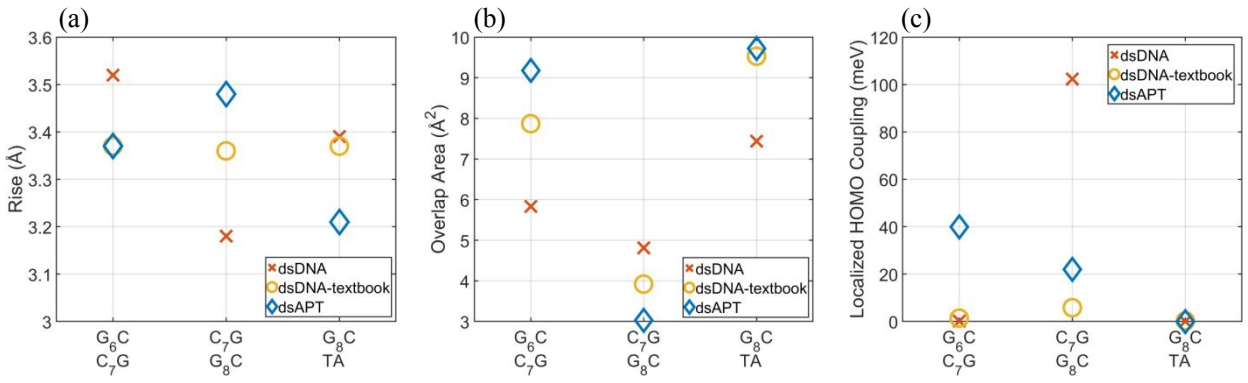

Figure 9 Rise, overlap, and localized HOMO coupling plots between the nearest neighboring base-pairs $G_6C_7G_8T$, respectively.

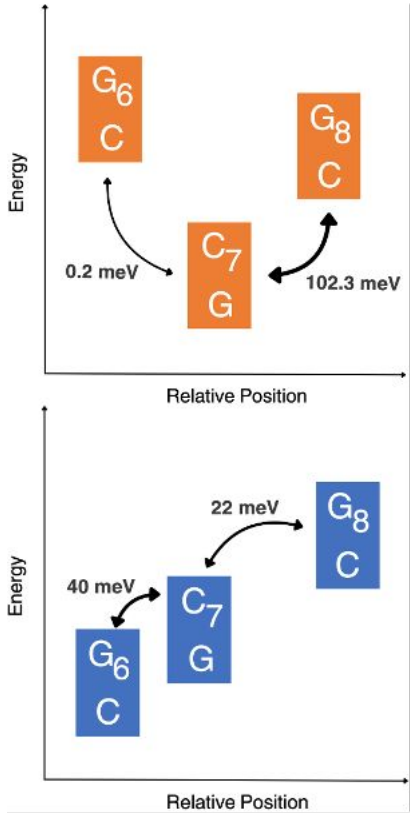

Figure 10 Overall picture of the aptamer effect on the DNA structure and its localized HOMO coupling. ***Top*** *dsDNA without aptamer,* ***Bottom*** *DNA+aptamer.*

6 Conclusion

Using DNA in electrical applications is driven by the progress of conductance measurement techniques employing the contact-DNA-contact setup. Modifying the conductance of DNA through binding of molecules opens the possibilities of creating future molecular-electronic devices. DNA aptamer is an already established method for creating biosensors as it binds to target molecules. In this work, we studied the electronic and structural effects of aptamer binding to ds-DNA within a contact-DNA-contact setup. We modeled a 12 bp dsDNA with a G-quadruplex aptamer binding to it through a TTTAA bridge DNA segment. We used a combination of MD simulations, DFT, and Green's function-based charge transport calculations. Our results show that while the aptamer energy levels do not contribute to charge transport across the dsDNA within the HOMO region, it structurally affects the dsDNA. The aptamer modifies the distances between the three GC base-pairs segment closest to the binding site, enhancing their electronic coupling and creating a conductive path near the HOMO edge. The combined effects result in a large modulation of conductance by at least 47 times when compared with the dsDNA without the aptamer. The findings of this study can help evolve future techniques for utilizing DNA in molecular electronics, such as creating high-versus-low currents that comprise the two-bit states of zero and one. Further, it helps us create electrical-based biosensors using the contact-DNA-contact method.

7 Author Contribution

H. M. conceptualization, methodology, investigation, writing – original draft, formal analysis, supervision; L. A. formal analysis, visualization, writing – original draft; A. A. formal analysis, visualization, writing – original draft; O. A. methodology, formal analysis, visualization, writing – original draft; T. T. conceptualization, resources; M. P. A. , Writing – review & editing; T. N. conceptualization, resources, Writing – review & editing.

8 Conflicts of Interest

There are no conflicts to declare.

9 Acknowledgement

We would like to thank Busra Demir currently employed at Unilever R&D Port Sunlight, and William Livernois from the University of Washington, for their help with discussions on the MD process and building the structure. We also thank Arpan De from the University of Washington for his fruitful discussion on the MD simulation analysis. Olaiyan Alolaiyan further acknowledges King Abdulaziz City for Science and Technology fellowship.

10 References

1 P. W. K. Rothemund, *Nature 2006 440:7082*, 2006, **440**, 297–302.

2 B. Wei, M. Dai and P. Yin, *Nature 2012 485:7400*, 2012, **485**, 623–626.

3 Y. Ke, S. M. Douglas, M. Liu, J. Sharma, A. Cheng, A. Leung, Y. Liu, W. M. Shih and H. Yan, DOI:10.1021/ja906381y.

4 Y. Li, J. M. Artés, B. Demir, S. Gokce, H. M. Mohammad, M. Alangari, M. P. Anantram, E. E. Oren and J. Hihath, *Nat Nanotechnol*, 2018, **13**, 1167–1173.

5 A. K. Mahapatro, K. J. Jeong, G. U. Lee and D. B. Janes, *Nanotechnology*, 2007, **18**, 195202.

6 J. Hihath, S. Guo, P. Zhang and N. Tao, *Journal of Physics: Condensed Matter*, 2012, **24**, 164204.

7 B. Xu, P. Zhang, X. Li and N. Tao, *Nano Lett*, 2004, **4**, 1105–1108.

8 Y. Li, J. M. Artés and J. Hihath, *Small*, 2016, **12**, 432–437.

9 J. M. Artés, Y. Li, J. Qi, M. P. Anantram and J. Hihath, *Nat Commun*, 2015, **6**, 8870.

10 Y. Li, J. M. Artés, J. Qi, I. A. Morelan, P. Feldstein, M. P. Anantram and J. Hihath, *J Phys Chem Lett*, 2016, **7**, 1888–1894.

11 H. M. Berman and P. R. Young, 1981, preprint, DOI: 10.1146/annurev.bb.10.060181.000511.

12 C. B. Carlson, M. Vuyisich, B. D. Gooch and P. A. Beal, *Chem Biol*, 2003, **10**, 663–672.

13 X. Wang, L. Gao, B. Liang, X. Li and X. Guo, *J Mater Chem B*, 2015, **3**, 5150–5154.

14 C. Guo, K. Wang, E. Zerah-Harush, J. Hamill, B. Wang, Y. Dubi and B. Xu, *Nat Chem*, 2016, **8**, 484–490.

15 L. Zhang, S. Kaneko, S. Fujii, M. Kiguchi and T. Nishino, *Chemical Communications*, 2021, **57**, 4380–4383.

16 H. Mohammad, B. Demir, C. Akin, B. Luan, J. Hihath, E. E. Oren and M. P. Anantram, *Nanoscale Horiz*, 2021, **6**, 651–660.

17 C. Hght, M. G. Cardozo and A. J. Hopfinger, *Molecular Mechanics and Molecular Dynamics Studies of the Intercalation of Dynemicin-A with Oligonucleotide Models of DNA*, .

18 T. Harashima, C. Kojima, S. Fujii, M. Kiguchi and T. Nishino, *Chemical Communications*, 2017, **53**, 10378–10381.

19 T. Bayrak, S. Helmi, J. Ye, D. Kauert, J. Kelling, T. Schönherr, R. Weichelt, A. Erbe and R. Seidel, *Nano Lett*, 2018, **18**, 2116–2123.

20 C. Liu, L. Guo, B. Zhang and L. Lu, *RSC Adv*, 2019, **9**, 31636–31644.

21 E. Wierzbinski, A. de Leon, X. Yin, A. Balaeff, K. L. Davis, S. Reppireddy, R. Venkatramani, S. Keinan, D. H. Ly, M. Madrid, D. N. Beratan, C. Achim and D. H. Waldeck, *J Am Chem Soc*, 2012, **134**, 9335–9342.

22 R. D. Teo, E. R. Smithwick and A. Migliore, *Physical Chemistry Chemical Physics*, 2019, **21**, 22869–22878.

23 M. Fuentes-Cabrera, X. Zhao, P. R. C. Kent and B. G. Sumpter, *J Phys Chem B*, 2007, **111**, 9057–9061.

24 L. Zhang, L. Zhou, J. Tian and X. Li, *Chem Phys Lett*, 2014, **597**, 69–74.

25 A. De, H. Mohammad, Y. Wang, R. Kubendran, A. K. Das and M. P. Anantram, *Sci Rep*, 2023, **13**, 6650.

26 Y. Zhang, S. Z. Chen, Z. X. Xie, X. Yu, Y. X. Deng, X. H. Chen and F. Ning, *Physics Letters, Section A: General, Atomic and Solid State Physics*, 2019, **383**, 2069–2075.

27 N. Kang, A. Erbe and E. Scheer, *Appl Phys Lett*, 2010, **96**, 94–97.

28 Y. Zhang, R. M. Young, A. K. Thazhathveetil, A. P. N. Singh, C. Liu, Y. A. Berlin, F. C. Grozema, F. D. Lewis, M. A. Ratner, N. Renaud, K. Siriwong, A. A. Voityuk, M. R. Wasielewski and D. N. Beratan, *Journal of Physical Chemistry Letters*, 2015, **6**, 2434–2438.

29 L. Xiang, J. L. Palma, Y. Li, V. Mujica, M. A. Ratner and N. Tao, *Nat Commun*, 2017, **8**, 1–10.

30 R. Sha, L. Xiang, C. Liu, A. Balaeff, Y. Zhang, P. Zhang, Y. Li, D. N. Beratan, N. Tao and N. C. Seeman, *Nature Nanotechnology 2018 13:4*, 2018, **13**, 316–321.

31 S. Vecchioni, B. Lu, W. Livernois, Y. P. Ohayon, J. B. Yoder, C. Yang, K. Woloszyn, W. Bernfeld, M. P. Anantram, J. W. Canary, W. A. Hendrickson, L. J. Rothschild, C. Mao, S. J. Wind, N. C. Seeman and R. Sha, *Advanced Materials*, DOI:10.1002/adma.202210938.

32 S. R. Patil, H. Mohammad, V. Chawda, N. Sinha, R. K. Singh, J. Qi and M. P. Anantram, *ACS Appl Nano Mater*, 2021, **4**, 10029–10037.

33 B. Sequeira-Antunes and H. A. Ferreira, *Biomedicines*, 2023, **11**, 3201.

34 D. Li, S. Song and C. Fan, *Acc Chem Res*, 2010, **43**, 631–641.

35 V. Valsangkar, S. Vangaveti, G. W. Lee, W. M. Fahssi, W. S. Awan, Y. Huang, A. A. Chen and J. Sheng, *Molecules*, DOI:10.3390/molecules26154620.

36 M. Z. Sabri, A. A. A. Hamid, S. M. S. Hitam and M. Z. A. Rahim, *Biophys Chem*, DOI:10.1016/j.bpc.2020.106492.

37 C. H. Yu, B. Ge, D. Sen and H. Z. Yu, *J Am Chem Soc*, 2008, **130**, 8023–8029.

38 B. Deng, Y. Lin, C. Wang, F. Li, Z. Wang, H. Zhang, X.-F. Li and X. C. Le, *Anal Chim Acta*, 2014, **837**, 1–15.

39 P. B. Woiczikowski, T. Kubař, R. Gutiérrez, G. Cuniberti and M. Elstner, *J Chem Phys*, DOI:10.1063/1.3460132.

40 E. Shapir, L. Sagiv, T. Molotsky, A. B. Kotlyar, R. Di Felice and D. Porath, *The Journal of Physical Chemistry C*, 2010, **114**, 22079–22084.

41 C. H. Yu, B. Ge, D. Sen and H. Z. Yu, *J Am Chem Soc*, 2008, **130**, 8023–8029.

42 W. Saenger, W. N. Hunter and O. Kennard, *Nature*, 1986, **324**, 385–388.

43 M. Alangari, B. Demir, C. A. Gultakti, E. E. Oren and J. Hihath, *Biomolecules*, 2023, **13**, 129.

44 T. Kubař and M. Elstner, *Journal of Physical Chemistry B*, 2008, **112**, 8788–8798.

45 K. Zheng, Z. Chen, Y. Hao and Z. Tan, *Nucleic Acids Res*, 2010, **38**, 327–338.

46 D. N. Edwards, A. Machwe, Z. Wang and D. K. Orren, *PLoS One*, 2014, **9**, e80664.

47 G. J. Myres, J. P. Kitt and J. M. Harris, *Anal Chem*, 2023, **95**, 16160–16168.

48 D. Bhattacharyya, G. Mirihana Arachchilage and S. Basu, *Front Chem*, DOI:10.3389/fchem.2016.00038.

49 D. A. Nicholson and D. J. Nesbitt, *J Phys Chem B*, 2023, **127**, 6842–6855.

50 S. L. Noer, S. Preus, D. Gudnason, M. Aznauryan, J.-L. Mergny and V. Birkedal, *Nucleic Acids Res*, 2016, **44**, 464–471.

51 M. D. Hanwell, D. E. Curtis, D. C. Lonie, T. Vandermeersch, E. Zurek and G. R. Hutchison, *J Cheminform*, 2012, **4**, 17.

52 R. Dennington, T. A. Keith and J. M. Millam, *Semichem Inc.*, 2019, preprint, Semichem Inc.:6.

53 D. A. Case, R. M. Betz, D. S. Cerutti, C. I. T.E., T. A. Darden, R. E. Duke, T. J. Giese, H. Gohlke, A. W. Goetz, N. Homeyer, S. Izadi, P. Janowski, J. Kaus, A. Kovalenko, T. S. Lee, S. LeGrand, P. Li, C.Lin, T. Luchko, R. Luo, B. Madej, D. Mermelstein, K. M. Merz, G. Monard, H. Nguyen, H. T. Nguyen, I. Omelyan, A. Onufriev, D. R. Roe, A. Roitberg, C. Sagui, C. L. Simmerling, W. M. Botello-Smith, J. Swails, R. C. Walker, J. Wang, R. M. Wolf, X. Wu, L. Xiao and P. A. Kollman, *University of California, San Francisco*.

54 I. Ivani, P. D. Dans, A. Noy, A. Pérez, I. Faustino, A. Hospital, J. Walther, P. Andrio, R. Goñi, A. Balaceanu, G. Portella, F. Battistini, J. L. Gelpí, C. González, M. Vendruscolo, C. A. Laughton, S. A. Harris, D. A. Case and M. Orozco, *Nat Methods*, DOI:10.1038/nmeth.3658.

55 W. L. Jorgensen, J. Chandrasekhar, J. D. Madura, R. W. Impey and M. L. Klein, *J Chem Phys*, 1983, **79**, 926–935.

56 S. Miyamoto and P. A. Kollman, *J Comput Chem*, 1992, **13**, 952–962.

57 T. Darden, D. York and L. Pedersen, *J Chem Phys*, DOI:10.1063/1.464397.

58 W. Humphrey, A. Dalke and K. Schulten, *J Mol Graph*, DOI:10.1016/0263-7855(96)00018-5.

59 D. J. Frisch, M. J.; Trucks, G. W.; Schlegel, H. B.; Scuseria, G. E.; Robb, M. A.; Cheeseman, J. R.; Scalmani, G.; Barone, V.; Petersson, G. A.; Nakatsuji, H.; Li, X.; Caricato, M.; Marenich, A. V.; Bloino, J.; Janesko, B. G.; Gomperts, R.; Mennucci, B.; Hratch, *Gaussian, Inc., Wallingford CT*, 2016, preprint.

60 Y. Wang, B. Demir, H. Mohammad, E. E. Oren and M. P. Anantram, *Phys Rev E*, 2023, **107**, 044404.

61 D. Valverde, A. Vasconcelos Sanches de Araujo, A. Carlos Borin and S. Canuto, *Physical Chemistry Chemical Physics*, 2017, **19**, 29354–29363.

62 A. Halder, A. Datta, D. Bhattacharyya and A. Mitra, *J Phys Chem B*, 2014, **118**, 6586–6596.

63 I. A. Uddin, E. Stec and G. A. Papadantonakis, *ChemPhysChem*, DOI:10.1002/cphc.202300946.

64 R. D. Teo, K. Terai, A. Migliore and D. N. Beratan, *Physical Chemistry Chemical Physics*, 2018, **20**, 26063–26067.

65 H. Mohammad and M. P. Anantram, *Phys Rev E*, 2023, **108**, 044403.

66 P.-O. Löwdin, *J Chem Phys*, 1950, **18**, 365–375.

67 C. J. O. Verzijl, J. S. Seldenthuis and J. M. Thijssen, *Journal of Chemical Physics*, DOI:10.1063/1.4793259.

68 J. L. D'Amato and H. M. Pastawski, *Phys Rev B*, 1990, **41**, 7411–7420.

69 M. Buttiker, *IBM J Res Dev*, 1988, **32**, 63–75.

70 J. Qi, M. G. Rabbani, S. Edirisinghe and M. P. Anantram, *Proceedings of the IEEE Conference on Nanotechnology*, 2011, 487–491.

71 C. Adessi, S. Walch and M. P. Anantram, *Phys Rev B Condens Matter Mater Phys*, 2003, **67**, 1–4.

72 F. Zahid, M. Paulsson and S. Datta, in *Advanced Semiconductor and Organic Nano-Techniques*, Elsevier Inc., 2003, pp. 1–41.

73 T. Caruso, M. Carotenuto, E. Vasca and A. Peluso, *J Am Chem Soc*, 2005, **127**, 15040–15041.

74 T. Caruso, A. Capobianco and A. Peluso, *J Am Chem Soc*, 2007, **129**, 15347–15353.

75 T. Nishino and P. T. Bui, *Chemical Communications*, 2013, **49**, 3437.

76 T. Lu and F. Chen, *J Comput Chem*, 2012, **33**, 580–592.

77 T. Lu, *Journal of Chemical Physics*, 2024, **161**, 82503.

78 J. Qi, N. Edirisinghe, M. G. Rabbani and M. P. Anantram, *Phys Rev B Condens Matter Mater Phys*, 2013, **87**, 1–10.

79 X. J. Lu and W. K. Olson, *Nucleic Acids Res*, 2003, **31**, 5108–5121.

Data Availability Statement

The data supporting this article have been included as part of the Supplementary Information.